Journal of Materials Chemistry A

ROYAL SOCIETY OF CHEMISTRY

PAPER

View Article Online
View Journal | View Issue

Cite this: J. Mater. Chem. A, 2023, 11, 14108

A comprehensive investigation of the $(Ti_{0.5}Zr_{0.5})_1(Fe_{0.33}Mn_{0.33}Cr_{0.33})_2$ multicomponent alloy for room-temperature hydrogen storage designed by computational thermodynamic tools†

Jéssica Bruna Ponsoni, [ab] Mateusz Balcerzak, *[bc] Walter José Botta, [ad] Michael Felderhoff [b] and Guilherme Zepon *[ad]

Multicomponent alloys with C14 Laves phase structures are promising hydrogen storage materials because of their ability to reversibly absorb substantial amounts of hydrogen at room temperature with good kinetics, long cycling life, and easy activation. The applicability of these alloys as hydrogen storage media is governed by their thermodynamic properties, which can be tuned by the design of the chemical composition, as well as electronic and geometrical factors. In this work, the $(Ti_{0.5}Zr_{0.5})_1(Fe_{0.33}Mn_{0.33}Cr_{0.33})_2$ alloy was designed using computational thermodynamic tools. CALPHAD calculation predicted that this alloy would solidify as a single C14 Laves phase. Moreover, the calculation of the pressure–composition–temperature (PCT) diagram, using a recently developed thermodynamic model, indicated that it would present mild hydrogen equilibrium pressure (~12 bar) at room temperature. The calculated hydrogen equilibrium pressure in the order of 10^1 bar would enable this alloy to store hydrogen at room temperature reversibly. The alloy was synthesized by arc-melting, and X-ray powder diffraction (XRD) demonstrated that the alloy indeed solidified as a single C14 Laves phase. The thermodynamic properties of the alloy during the hydrogen absorption and desorption processes were experimentally investigated by the acquisition of PCT diagrams. The alloy absorbs at room temperature a large amount of hydrogen (up to 1 H/M; ~1.7 wt%) under moderate hydrogen equilibrium pressures and with fast kinetics. Furthermore, it was demonstrated that the alloy reversibly absorbs and desorbs the total amount of hydrogen (H/M = 1) at room temperature with excellent cycling stability.

Received 12th April 2023
Accepted 26th May 2023

DOI: 10.1039/d3ta02197a

rsc.li/materials-a

Introduction

Hydrogen is a strategic renewable and clean energy carrier that offers solutions to the key technologies of a future sustainable economy. However, for the use of hydrogen to be efficient and cost-effective, significant challenges must be overcome, especially in terms of safe and compact storage and transportation. Regarding applicability, different hydrogen storage methods such as gas-, liquid- and solid-state were investigated and compared. Solid-state storage through metal hydrides (MH) has proven to be an excellent alternative to the other available methods, providing reversibility, safety, and high volumetric storage capacities. Therefore, MHs can be strategically used in some applications as tanks for solid-state hydrogen storage, heat-storage systems, heat pumps, fuel cells, and batteries.[1,2] In this regard, high entropy alloys (HEA), multi-principal element alloys (MPEA), complex concentrated alloys (CCA), or, more generally, multicomponent alloys significantly expanded the number of potential chemical compositions that should be assessed to find alloys with optimized hydrogen storage properties for any hydrogen storage application.

Multicomponent alloys for hydrogen storage have been classified as body-centered cubic (BCC), lightweight, and intermetallic multicomponent alloys.[3] Among the intermetallic multicomponent alloys, the Laves phases have been identified as the most common.[4] Furthermore, as reported by some studies, Laves phase alloys have been considered promising hydrogen storage materials due to their ability to reversibly absorb substantial amounts of hydrogen with good kinetics, long cycling life, easy activation, and relatively low-cost

[a]Graduate Program in Materials Science and Engineering (PPGCEM/UFSCar), Federal University of Sao Carlos, Rodovia Washington Luiz, km 235, São Carlos, São Paulo CEP, 13565-905, Brazil. E-mail: zepon@ufscar.br

[b]Department of Heterogeneous Catalysis, Max-Planck-Institut für Kohlenforschung, Kaiser-Wilhelm Platz 1, Mülheim an der Ruhr, 45470, Germany. E-mail: balcerzak@kofo.mpg.de

[c]Institute of Materials Science and Engineering, Poznan University of Technology, Jana Pawła II No 24, Poznan 61-138, Poland

[d]Department of Materials Engineering (DEMa/UFSCar), Federal University of São Carlos, Rodovia Washington Luiz, km 235, São Carlos CEP, 13565-905, Brazil

† Electronic supplementary information (ESI) available. See DOI: https://doi.org/10.1039/d3ta02197a

materials. In addition, most works that report the functional properties of multicomponent alloys deal with single Laves phase structures.[4–9]

The Laves phases are classified into three structures: hexagonal $MgZn_2$-, cubic $MgCu_2$-, or hexagonal $MgNi_2$-type structures, namely C14, C15, and C36, respectively. The C14 Laves phase is the most common among them.[4] The intermetallic compound for hydrogen storage is typically designed by combining a strong hydride-forming element (A elements) and a non-stable hydride-forming one (B elements). The classification of A- and B-type elements is related to the interaction of the individual elements with hydrogen, *i.e.*, by the enthalpy of hydride formation. A-type elements have low values (more negative) of enthalpy of hydride formation and a higher tendency to form a hydride phase. B-type elements have high values of enthalpy of hydride formation (less negative or even positive), which results in a lower affinity with hydrogen.[3,10]

Among the AB_2-type Laves phase alloys, the $TiMn_2$ system has been extensively studied due to its attractive hydrogen storage capacity.[11,12] Furthermore, partial substitutions of the A and/or B elements by other elements such as Zr, Nb, V, Cr, Fe, Co, and Ni have been the primary strategy to improve the hydrogen storage properties of this alloy.[5,6,11–16]

Because of the vast compositional field of multicomponent alloys, different strategies have been proposed to design alloy compositions with optimized hydrogen storage properties for various applications. Recently, we presented an approach to design multicomponent alloys with C14 Laves phase structure for hydrogen storage based on empirical and thermodynamic models.[17] The empirical model considered geometrical and electronic factors, usually associated with the formation and stability of multicomponent Laves phase, based on the chemical alloy composition, such as the valence electron concentration (VEC), atomic radius ratio between A- and B-type elements (r_A/r_B), and atomic size mismatch (δ) calculated by eqn (1).

$$\delta = \sqrt{\sum c_i \left(1 - \frac{r_i}{\bar{r}}\right)^2 \times 100} \quad (1)$$

where c_i and r_i are the atomic fraction of element i, r_i is the atomic radius of element i, and $\bar{r} = \sum c_i r_i$ is the mean atomic radius of all elements in the alloy.

In addition, the Calculation of Phase Diagrams (CALPHAD) method was applied as a thermodynamic-based tool to predict phase formation and stability of the alloy compositions. Furthermore, a thermodynamic model was developed to calculate PCT diagrams of multicomponent C14-type Laves phase alloys, which made it possible to determine pressure–temperature operation conditions for the designed alloys.

The present work shows the results of the studies run on an alloy with the chemical composition selected by the recently proposed alloy design approach. The selected alloy was designed aiming at room temperature absorption/desorption under moderate hydrogen pressure with good capacity and reversibility. The $(Ti_{0.5}Zr_{0.5})_1(Fe_{0.33}Mn_{0.33}Cr_{0.33})_2$ alloy was chosen and experimentally investigated in terms of its crystal structure and hydrogen storage performance concerning hydrogen capacity, kinetics of absorption/desorption, and cycling reversibility and stability.

Alloy design

The $(Ti_{0.5}Zr_{0.5})_1(Fe_{0.33}Mn_{0.33}Cr_{0.33})_2$ composition was selected based on the design strategy reported by Ponsoni *et al.*,[17] which focused on finding C14 Laves phase alloys based on a high-throughput calculation of electronic and geometrical factors (VEC, r_A/r_B, and δ) and CALPHAD calculations of these alloys (Thermo-Calc™ software and TCHEA5 database). One of the alloys designed in this recent report[17] that showed potential for room temperature hydrogen storage is the $(Ti_{0.5}Zr_{0.5})_1(Fe_{0.33}Mn_{0.33}Cr_{0.33})_2$ alloy, which was experimentally investigated in the present work. Fig. 1 shows the mole fraction of equilibrium phases as a function of temperature calculated by CALPHAD for $(Ti_{0.5}Zr_{0.5})_1(Fe_{0.33}Mn_{0.33}Cr_{0.33})_2$ composition. The thermodynamic calculation indicates that under equilibrium conditions, the alloy solidifies as a primary C14 Laves phase. Moreover, it is predicted that a minor fraction of the BCC phase (<1%) forms in the final stage of the solidification at approximately 1330 °C. Upon cooling to lower temperatures (<900 °C), the formation of a C15 Laves phase and other cubic phases is also predicted. Nonetheless, the formation of the cubic phases might be suppressed due to the high cooling rate imposed in the alloy synthesis process.

In this AB_2-type system, the A elements are Ti and Zr, and the B elements are Fe, Mn, and Cr. Table 1 shows the values of the alloy's VEC, r_A/r_B, δ, and its molar mass. The values of VEC, r_A/r_B, and δ are within the range of values with the highest incidence of the C14 Laves phase observed in the study of a total of 1208 compositions, *i.e.*, $5.8 \leq \text{VEC} \leq 7.0$, $1.1233 \leq r_A/r_B \leq 1.223$ and $\delta > 5\%$.[17] Although these electronic and geometric factors alone are insufficient to explain the formation and stability of the Laves phase, they play an essential role in predicting the Laves phase formation. They are widely discussed in the literature.[9,18–22]

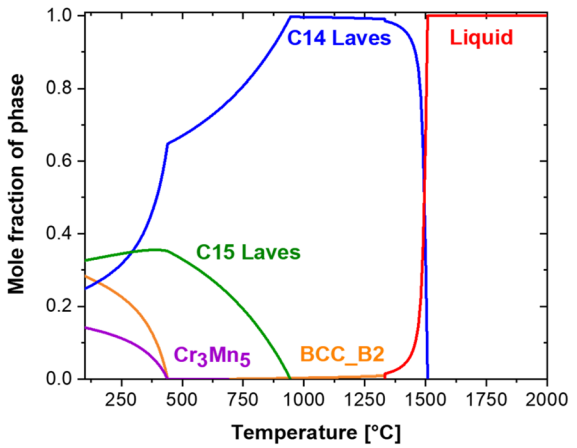

Fig. 1 Mole fraction of equilibrium phases as a function of temperature calculated by CALPHAD for the $(Ti_{0.5}Zr_{0.5})_1(Fe_{0.33}Mn_{0.33}Cr_{0.33})_2$ alloy.

Table 1 VEC, r_A/r_B, δ and molar mass of the $(Ti_{0.5}Zr_{0.5})_1(Fe_{0.33}Mn_{0.33}Cr_{0.33})_2$ alloy

VEC	r_A/r_B	δ	MM [g mol^{-1}]
6.0	1.205	9.52	59.36

Furthermore, the design strategy reported by Ponsoni *et al.*[17] presents a thermodynamic model to calculate PCT diagrams for the C14 Laves phase alloys, hereafter called the PCT-C14 model, for the sake of conciseness.

The PCT-C14 model estimates the enthalpy and entropy of hydrogen solution in the C14 Laves phase by applying the necessary considerations regarding the C14 Laves phase structure and available interstitial sites for hydrogen absorption. The PCT-C14 modelling considers the hydrogen-multicomponent alloy system under para-equilibrium (PE) conditions. PE is a type of thermodynamic equilibrium observed in most hydrogen storage systems working at low or moderate temperatures, in which the mobility of the metal atoms is limited. It can be assumed that the metal atoms are "frozen". In contrast, only the hydrogen atoms have enough mobility to change the chemical composition of the phases. In these circumstances, an equilibrium condition is attained because hydrogen mobility allows the chemical potential of hydrogen to be the same in all the co-existing phases, resulting in a minimum free energy of the system ($\Delta G_m(c_H)$). It is important to emphasize that this model is a further development of the thermodynamic model first proposed by Zepon *et al.*[23] for calculating PCT diagrams for multicomponent BCC alloys.

The crystal structure of the C14 Laves phase is hexagonal with space group $P6_3/mmc$. The structure contains twelve atoms and four AB_2 formula units per unit cell. The A-type atoms occupy the 4f (A_1) Wyckoff position, and the B-type atoms occupy the 2a (B_1) and 6h (B_2) Wyckoff positions. For the AB_2 system studied in this work, the A-type elements, Ti and Zr, occupy A_1 positions, while B-type elements, Fe, Mn, and Cr, occupy B_1 and B_2 positions. Furthermore, three types of tetrahedral interstitial sites exist in the C14-type Laves phase: A_2B_2, AB_3, and B_4. The C14 structure has 12 equivalent A_2B_2 interstitial sites, four equivalent AB_3 interstitial sites, and one B_4 interstitial site per formula unit, totaling 68 tetrahedral interstitial sites per unit cell.

The PCT-C14 model considers that the hydrogen atoms will form an interstitial solid solution only in the A_2B_2 interstitial sites, which are more energetically favorable, and the maximum hydrogen capacity will be H/M = 1. The unit cell of the hexagonal C14 Laves phase and the tetrahedral interstices are illustrated in Fig. S1 in the ESI.†

In the PCT-C14 model, the authors considered that the enthalpy of the C14 Laves phase ($\Delta H_m(c_H)$) varies linearly with the hydrogen content. A detailed description of the calculation method of the thermodynamic model and its advantages and limitations can be found in the study reported by Ponsoni *et al.*[17] In summary, the PCI curves can be calculated using eqn (2).[17]

$$\ln\left(\frac{P_{H_2}}{p^0}\right) = \frac{2}{RT}\left(h_{C14} - T\left[-R\ln\left(\frac{c_H}{1-c_H}\right) - \frac{S^\circ_{H_2}}{2}\right]\right) \quad (2)$$

where $p^0 = 1$ atm is the reference state, P_{H_2} is a given hydrogen pressure, R is the ideal gas constant, and T is a given temperature. $c_H = \frac{n_H}{n_M}$ is the amount of hydrogen in the phase, where n_H and n_M are the number of mol of hydrogen and metal atoms in the phase, respectively. $S^\circ_{H_2}$ is the standard entropy of H_2 gas, which is given by eqn (3).[23]

$$S^\circ(H_2) = A\ln(t) + Bt + \frac{Ct^2}{2} + \frac{Dt^3}{3} + \frac{Et^{-2}}{2} + G(\text{J per mol of } H_2) \quad (3)$$

where $t = T$ (K)/100, $A = 33.066178$, $B = -11.363417$, $C = 11.432816$, $D = -2.772874$, $E = -0.158558$, and $G = 172.707974$. It is worth noting that eqn (2) is only valid between 298 K and 1000 K. h_{C14} is the hydrogen partial molar enthalpy of the C14 Laves phase. Some alloys with Laves C14 phase present PCI curves with plateau pressure, suggesting that a phase equilibrium between a low hydrogen content solid solution and high hydrogen content hydride occurs for these alloys.[5,7,15] However, the thermodynamic model applied in this study considers that the alloy absorbs hydrogen only by solid solution, which results in the absence of a well-defined plateau pressure, as reported in several studies.[6,8,24] In this way, h_{C14} was described as a sum of the contribution of each element in the A_2B_2 tetrahedral sites, which were considered the only ones occupied by hydrogen. The contribution of the hydrogen partial molar of each alloy element i was approximated by its enthalpy of hydrogen solution at infinite dilution (ΔH_i^∞). Therefore, h_{C14} was described as eqn (4).[17]

$$h_{C14} = \frac{1}{2}\sum_i c_i^A \Delta H_i^\infty + \frac{1}{2}\sum_i c_i^B \Delta H_i^\infty \quad (4)$$

where c_i^A is the atomic fraction of element i in the A sublattice, and c_i^B is the atomic fraction of element i in the B sublattice (therefore, $\sum c_i^A = \sum c_i^B$). Experimental values of ΔH_i^∞ are reported by R. Griessen, T. Riesterer,[25] and the values for the alloy elements in kJ mol^{-1} H are $\Delta H_{Ti}^\infty = -52$, $\Delta H_{Zr}^\infty = -52$, $\Delta H_{Fe}^\infty = 29$, $\Delta H_{Mn}^\infty = 1$, and $\Delta H_{Cr}^\infty = 28$.

The $(Ti_{0.5}Zr_{0.5})_1(Fe_{0.33}Mn_{0.33}Cr_{0.33})_2$ alloy is characterized by $h_{C14} = -16.33$ kJ mol^{-1} H, and the calculated PCI curves for the $(Ti_{0.5}Zr_{0.5})_1(Fe_{0.33}Mn_{0.33}Cr_{0.33})_2$ alloy at 30 °C, 60 °C, 90 °C, and 130 °C are shown in Fig. 2.

The applicability of an alloy as a hydrogen storage material is intrinsically related to its PCT diagram, which determines the maximum hydrogen storage capacity and pressure–temperature operation condition. For a solid-state hydrogen storage tank operating at room temperature and moderate pressure conditions, the alloy needs to have a set of properties, such as high hydrogen storage capacity, good absorption and desorption kinetics, cycling stability, reversibility, and the PCT diagram has to present an equilibrium pressure just above atmospheric pressure, for example, between 2 and 20 bar. Thereby, the pressure needed to charge the tank would be relatively low and far below the pressure used in typical commercial hydrogen gas

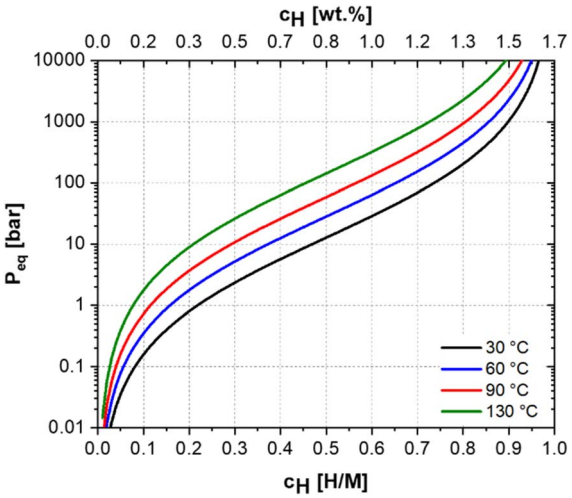

Fig. 2 Calculated PCT diagram for the $(Ti_{0.5}Zr_{0.5})_1(Fe_{0.33}Mn_{0.33}Cr_{0.33})_2$ C14 Laves phase alloy.

cylinders (≈200 bar). In addition, since the plateau pressure is above the atmospheric, the alloy might desorb the hydrogen at room temperature by simply reducing the system pressure.

Therefore, since the calculated PCT diagram for the $(Ti_{0.5}Zr_{0.5})_1(Fe_{0.33}Mn_{0.33}Cr_{0.33})_2$ alloy shows an equilibrium pressure of 12 bar for H/M = 0.5 at 30 °C, the alloy might reversibly absorb hydrogen at room temperature and be a potential candidate for solid-state hydrogen storage tank application operating under mild temperature–pressure conditions. In addition, this composition can be produced at a relatively low cost because of the high fraction of Cr (19.47 wt%), Mn (20.57 wt%), and Fe (20.91 wt%). Moreover, the high Cr content prevents alloy oxidation, an essential feature for hydrogen storage alloy.

Experimental procedures

Sample production

The $(Ti_{0.5}Zr_{0.5})_1(Fe_{0.33}Mn_{0.33}Cr_{0.33})_2$ alloy was produced from pure elements (purity > 99%) by arc-melting under an inert argon atmosphere. The titanium getter was melted before the alloy to reduce the oxygen content in the melting chamber. The sample was turned over and re-melted three times to ensure chemical homogeneity. The sample was stored in an argon-filled MBRAUM glovebox (H_2O and O_2 levels below 1 ppm).

Structure characterization

The structural characterization was conducted *via* XRD using an STOE STADI P transmission diffractometer with Mo radiation (0.7093 Å). The instrument is equipped with a primary Ge (111) monochromator ($MoK\alpha_1$) and a position-sensitive Mythen1K detector. Data were collected in the 2θ range between 5° and 50° with a step width of 0.015°. The measurement time per step was 20 s. The samples were filled into 0.3 mm diameter borosilicate glass capillaries for the XRD analysis. The XRD profiles were analyzed by the Rietveld refinement method using the GSAS-II software[26] to determine lattice parameters and phase fraction. The as-cast ingot sample was crushed inside an argon-filled MBRAUM glovebox (H_2O and O_2 levels below 1 ppm) using an agate mortar and pestle for the XRD measurements.

The microstructure characterization was performed by Scanning Electron Microscopy analysis (SEM), acquiring a back-scattered electron (BSE) signal using a Hitachi TM 3030 microscope with an accelerating voltage of 15 kV. The chemical composition was evaluated by Energy Dispersive Spectroscopy (EDX) using an Xplore Compact 30 Oxford detector in the SEM microscope. Before SEM-EDX analysis, the sample was embedded into resin and ground with SiC papers with mesh sizes of 180, 320, 400, 600, and 1200 followed by polishing in silica suspension.

Hydrogen storage characterization

For the hydrogen storage characterization, the as-cast ingot samples were crushed into powder inside a glovebox as previously described and loaded into a Sieverts-type apparatus (Setaram PCT Pro-version E&E). Approximately 1 g of the alloy powder was loaded into the sample holder. The sample was subjected to a heat treatment at 390 °C under a dynamic vacuum for 12 h before the measurements to avoid any deleterious effect of the hydrogen leak test performed before the experiments and ensure a good first hydrogenation. For the first hydrogen absorption kinetic measurement, the sample was cooled to 30 °C and exposed to hydrogen at 52 bar. Pressure–composition–isotherm (PCI) were obtained at 30 °C, 60 °C, 90 °C and 130 °C. The absorption and desorption PCI curves were recorded by applying doses of hydrogen up to the maximum pressure of 100 bar. After each measurement, the sample was exposed to a dynamic vacuum for a few minutes at the current temperature. For cycling experiments, the absorption kinetics were carried out under initial hydrogen pressures of 52 bar (reservoir plus sample holder with 30.54 cm^3) for 30 min. The desorption kinetics were carried out by reducing the hydrogen pressure in the sample to values below 1 bar and also lasted 30 min. Therefore, the sample was not exposed to a vacuum during the desorption kinetics measurements. The hydrogen gas was expanded into the apparatus's largest volume reservoir (1163.61 cm^3) to reach pressures below 1 bar. The alloy was subjected to fifty cycles of hydrogen absorption and desorption without air or vacuum exposure.

Results and discussion

Structural characterization

Fig. 3 presents the XRD pattern with the results of its Rietveld refinement for the as-cast $(Ti_{0.5}Zr_{0.5})_1(Fe_{0.33}Mn_{0.33}Cr_{0.33})_2$ alloy confirming that the alloy has C14 Laves phase structure. No reflections from a secondary phase can be observed. The crystal structure and a unit cell of the hexagonal C14 Laves phase of the studied alloy are shown in Table S1 and Fig. S1, respectively, in the ESI.† This crystal structure was used in the Rietveld refinement procedure. The lattice parameters obtained by the

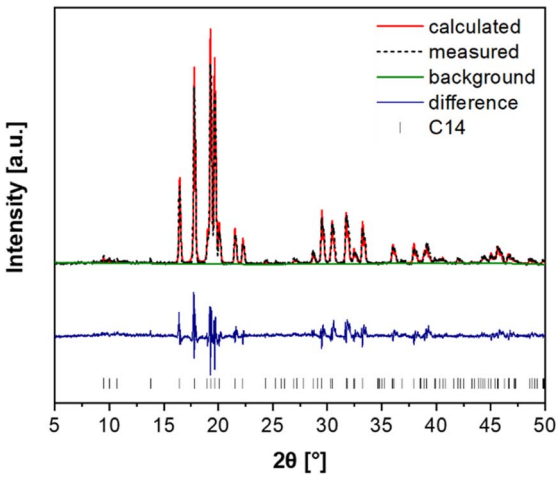

Fig. 3 Rietveld refinement of the XRD pattern of the as-cast $(Ti_{0.5}Zr_{0.5})_1(Fe_{0.33}Mn_{0.33}Cr_{0.33})_2$ indicating that the sample formed C14 Laves phase structure. No reflections from the secondary phase can be seen.

Rietveld refinement for the C14 Laves phase are $a = 0.496$ nm and $c = 0.814$ nm.

The alloy's microstructure was further investigated by SEM equipped with EDX, and the result is shown in Fig. 4. The as-cast sample presented a dendritic microstructure, as seen in the SEM-BSE image. EDX analyses were carried out in two selected areas: at the interdendritic regions (spectrum 1) and in the middle of dendrites (spectrum 2). The results of the overall chemical composition and the chemical composition in the dendritic and interdendritic regions are presented in Table 2. As can be seen, the overall composition of the alloy is very close to the nominal one. Ti and Zr are not homogeneously distributed between the dendritic and interdendritic regions as a result of segregation during solidification. On the other hand, Fe, Mn, and Cr appear uniformly distributed in both regions. The Mn content is generally slightly lower than the nominal one, which

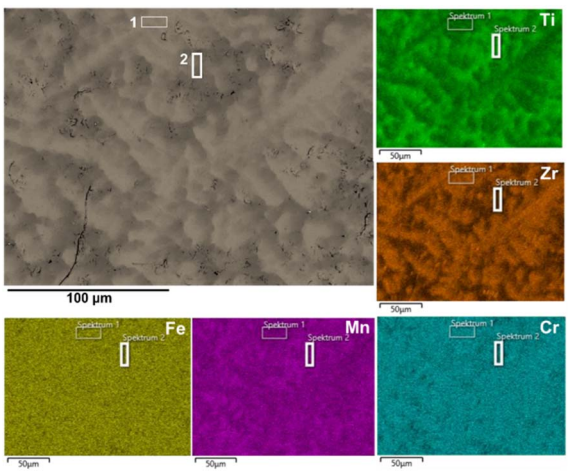

Fig. 4 SEM-BSE image and corresponding EDX elemental maps of the as-cast $(Ti_{0.5}Zr_{0.5})_1(Fe_{0.33}Mn_{0.33}Cr_{0.33})_2$ alloy.

Table 2 The chemical composition of the $(Ti_{0.5}Zr_{0.5})_1(Fe_{0.33}Mn_{0.33}Cr_{0.33})_2$ alloy determined by SEM-EDX

	Chemical composition in at% of the as-cast alloy				
Alloy	Ti	Zr	Fe	Mn	Cr
Nominal	16.67	16.67	22.22	22.22	22.22
Overall	17.90	17.34	21.90	20.57	22.30
Dendritic	22.09	13.89	21.26	21.88	20.89
Interdendritic	15.06	19.48	22.48	19.60	23.37

can be explained by its partial vaporization during the arc melting procedure due to its lower melting and boiling point and higher vapor pressure compared to the other alloying elements.

The chemical composition measured in the interdendritic region of the alloy is slightly richer in Zr and poorer in Ti. In contrast, the chemical composition measured in the middle of the dendrites is slightly richer in Ti and poorer in Zr. Nevertheless, the XRD analysis shows that the substitution behavior between Ti and Zr elements observed in regions 1 and 2 of the sample has no substantial influence on the alloy crystal structure. According to the XRD results, all the alloy regions have a C14 Laves phase structure, and no other phase can be observed. Furthermore, we can relate the slight broadening of the C14 Laves phase reflections to the minor deviations in the chemical composition of different alloy crystals. Those deviations lead to smaller or greater lattice parameters in different crystals (compared to the one of nominal $(Ti_{0.5}Zr_{0.5})_1(Fe_{0.33}Mn_{0.33}Cr_{0.33})_2$ alloy), resulting in the mentioned broadening.

Hydrogen storage properties

Kinetics and PCI measurements. The hydrogen storage performance of $(Ti_{0.5}Zr_{0.5})_1(Fe_{0.33}Mn_{0.33}Cr_{0.33})_2$ alloy was first investigated by absorption kinetic measurement at 30 °C as illustrated in Fig. 5. The alloy absorbs approximately 1.71 wt% of hydrogen, equivalent to H/M = 1.02, during the first absorption

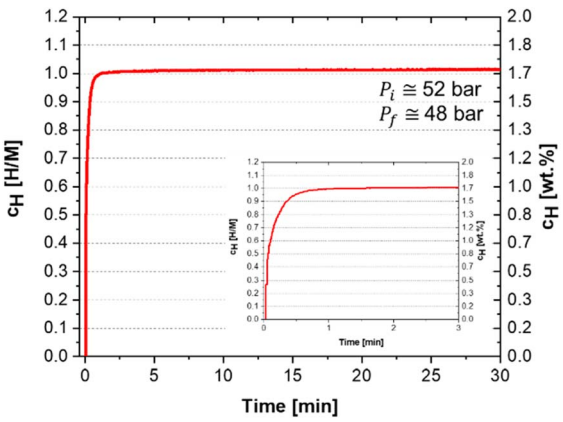

Fig. 5 Measurement of hydrogen absorption kinetics at 30 °C in H/M and wt% of the $(Ti_{0.5}Zr_{0.5})_1(Fe_{0.33}Mn_{0.33}Cr_{0.33})_2$ alloy under an initial hydrogen pressure $P_i = 52$ bar.

cycle under an initial hydrogen pressure of 52 bar. The inset in Fig. 5, which shows the first minutes of the process, confirms that the material absorbs hydrogen extremely fast, reaching 99% of the total hydrogen capacity in less than one minute. Similar kinetics behavior was observed for some reported alloys, such as TiZrCrFeMnNi,[5] $Ti_{0.8}Zr_{0.2}Mn_{0.9}Cr_{0.6}V_{0.3}M_{0.2}$ (M = Fe, Ni, Co),[15] and $Ti_{0.8}Zr_{0.2}Cr_{0.75}M_{1.25}Ce_{0.02}$.[27] It is important to mention that the alloy does not require any activation treatment to absorb hydrogen. The alloy was observed to absorb hydrogen during the necessary high-pressure hydrogen leak tests conducted prior to the start of the experiments. However, before the first absorption kinetics measurement, a heat treatment at 390 °C under a dynamic vacuum for 12 h was employed to ensure the sample was utterly hydrogen-free.

The hydrogen absorption and desorption performance of $(Ti_{0.5}Zr_{0.5})_1(Fe_{0.33}Mn_{0.33}Cr_{0.33})_2$ alloy was further evaluated by PCI measurements at 30 °C, 60 °C, 90 °C and 130 °C up to the maximum hydrogen pressure of 100 bar, as showed in Fig. 6. It is worth mentioning that the same sample was used for the measurements at four different temperatures. After each PCI measurement, the sample was exposed to a dynamic vacuum for a few minutes at the current temperature. Fig. 6 shows that the maximum hydrogen uptake at 100 bar decreases as the temperature increases: 1.75 wt% (H/M = 1.04), 1.66 wt% (H/M = 0.99), 1.56 wt% (H/M = 0.93), and 1.35 wt% (H/M = 0.81) for 30 °C, 60 °C, 90 °C, and 130 °C, respectively. For these temperatures, the observed hydrogen equilibrium pressures for the alloy having H/M = 0.5 were approximately 6, 13, 27, and 54 bar, respectively. Furthermore, the absence of a well-defined plateau pressure was observed in the PCI curves. As mentioned above, in the literature, experimental PCT diagrams of alloys crystalizing in a major C14 Laves phase are found in two typical shapes: with a flat plateau region with well-defined pressure and without a well-defined plateau pressure. These shapes are related to the occurrence or not, respectively, of phase separation between a low hydrogen content solid solution and high hydrogen content hydride. This phase separation might be understood as a hydrogen miscibility gap in the C14 Laves phase alloy, as discussed in detail by Ponsoni *et al.*[17] PCT curves with a well-defined plateau pressure were reported for the Laves phase alloys TiZrCrMnFeNi,[5] $Ti_{1-y}Cr_{2-x}Mn_x$,[7] $Ti_{0.8}Zr_{0.2}Mn_{0.9}Cr_{0.6}V_{0.3}M_{0.2}$ (M = Fe, Ni, Co)[15] and $(Ti_{0.8}Zr_{0.2})_{1.1}Mn_{1.2}Cr_{0.55}Ni_{0.2}V_{0.05}$.[28]

On the other hand, the absence of a well-defined plateau pressure suggests hydrogen absorption by interstitial solid solution, as considered in the development of the PCT-C14 model. This behavior was reported for the TiZrNbFeNi,[6] $Cr_uFe_vMn_wTi_xV_yZr_z$,[8] ZrTiVNiCrFe,[24] and $Ti_{0.5}Zr_{0.5}(V_{0.5}Ni_{1.1}Mn_{0.2}Fe_{0.2})_2$ (ref. 29) alloys.

It should be pointed out that the hydrogen storage capacity observed for the $(Ti_{0.5}Zr_{0.5})_1(Fe_{0.33}Mn_{0.33}Cr_{0.33})_2$ alloy in the kinetics and PCI measurements are quite close to the theoretical value of 1.67 wt% calculated considering the formation of an AB_2H_3 system. In addition, the PCI curves at the four measured temperatures presented minimal hysteresis. The sample could be desorbed almost entirely (H/M < 0.1) by reducing the hydrogen pressure to approximately 1 bar, even at 30 °C. Therefore, no temperature increase or vacuum is required to cycle this alloy. However, after each PCI measurement, the sample was exposed to a dynamic vacuum for a few minutes at the current temperature to ensure no remaining hydrogen was in the lattice. It is also worth mentioning that the decrease in the hydrogen absorption capacity of the alloy with the increasing temperature is related to the limitation of the maximum pressure achieved in the experiment. However, we believe hydrogen uptake would increase at higher temperatures if pressure above 100 bar was applied to the sample.

Although the experimental PCI curves do not show a well-defined plateau pressure, the van't Hoff plot was calculated for the pressure corresponding to c_H = H/M = 0.5. The van't Hoff plot and the thermodynamic data determined by it are shown in Fig. S2 and Table S2 in the ESI,† respectively.

The calculated and experimental PCI curves shown in Fig. 2 and 6, respectively, present differences in terms of shape, the equilibrium pressure and the maximum hydrogen uptake at 100 bar for the different temperatures. Fig. S3 in the ESI† compares experimental and calculated PCI curves. The differences between the calculated and experimental PCI curves are expected because of some simplifications of the PCT-C14 model employed. The S-shaped curves observed in the calculated PCIs (with the equilibrium pressure tending to infinity when H/M tends to unity) arise from the fact that the model considers that only 12 A_2B_2-type interstitial sites per unit cell are available for hydrogen occupation. Thus, when H/M approaches one, the model considers that almost all interstitial sites are occupied, yielding very high equilibrium pressure, which clearly differs from the experimental PCIs. In order to improve the predictability of the model in terms of PCI curve shape, some aspects should be considered in the thermodynamic description of $\Delta G_m(c_H)$. For instance, the PCT-C14 model assumes a random occupation of the A_2B_2-type interstitial sites by hydrogen atoms, which is the same as considering the occupation of interstitial sites with an average binding energy. However, the model does not consider that interstitial sites with lower binding energy

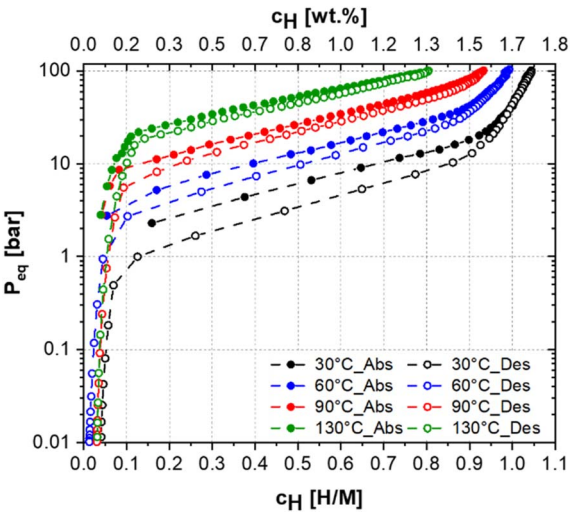

Fig. 6 PCIs of $(Ti_{0.5}Zr_{0.5})_1(Fe_{0.33}Mn_{0.33}Cr_{0.33})_2$ alloy at 30 °C, 60 °C, 90 °C and 130 °C.

may be more favourable to be occupied by hydrogen atoms than those with higher binding energy. This condition would result in a non-linear behaviour of $\Delta H_m(c_H)$ curve and would also change the configuration entropy component of the C14 Laves phase ($\Delta S_m(c_H)$). Moreover, by assuming that only 12 A_2B_2-type tetrahedral sites are available for hydrogen accommodation, the model does not consider the occupation of higher binding energy sites (AB_3- and B_4-type sites) especially at high temperatures, which is probable to occur in practice, resulting in a maximum hydrogen storage capacity higher than H/M = 1. Therefore, there is room for improvement of the model in this regard. Another simplification is that the hydrogen partial enthalpy for the C14 Laves phase is estimated by considering the enthalpy of hydrogen solution at infinite dilution of the pure elements in the A_2B_2-type tetrahedral sites. Therefore, no interaction between the atoms is being considered for estimating the enthalpy of hydrogen absorption in the C14 Laves phase. These aspects, which are out of the scope of this work, should be considered in future modelling and could result in an improvement in the predictions of the shape of the PCI curves, and consequently in an improved prediction of the hydrogen storage properties. However, despite the differences between calculation and experiment, the proposed model allowed us to quite reasonably determine the equilibrium pressure of the $(Ti_{0.5}Zr_{0.5})_1(Fe_{0.33}Mn_{0.33}Cr_{0.33})_2$ alloy as shown in Fig. 7.

The calculated equilibrium pressures were only slightly overestimated but were of the same order of magnitude as the experimental ones. Ponsoni *et al.*[17] reported that the equilibrium pressures for the C14-Laves phase can vary widely, from 10^{-4} up to 10^5 bar. Therefore, by combining the CALPHAD method and the thermodynamic model to calculate the PCT diagram for the C14 Laves phase, we could design an alloy composition with the equilibrium pressure in the targeted order of magnitude (10^1 bar), which would allow reversible absorption/desorption of hydrogen at room temperature. The experimental PCT diagram presented in Fig. 6 confirmed such reversibility. These thermodynamic computational tools are paramount to reducing the number of experiments to explore the vast compositional space of multicomponent alloys.

Reversibility and cycling performance. The hydrogen absorption/desorption cycling performance of the alloy was evaluated by measuring the hydrogen absorption capacity over 50 cycles. The results of the cycling test are shown in Fig. 8. The hydrogen absorption behavior was performed at 30 °C under an initial pressure of 52 bar for 30 min, while the hydrogen desorption was carried out at the same temperature under an initial pressure of approximately 0.6 bar for 30 min. Fig. 8(a) shows the hydrogen absorption and desorption curves for the 1st, 2nd, 10th, 20th, 30th, 40th, and 50th cycles. The hydrogen absorption capacity in the first cycle was 1.71 wt% (H/M = 1.02), decreased in the second cycle to 1.62 wt% (H/M = 0.97). This behavior can be justified by the size refinement of the alloy particles, which occurs during the first hydrogenation. The refinement of the particles might increase the crystalline defects, such as dislocations and grain boundaries, which are known to diminish the hydrogen storage content of metal hydrides.[15] Furthermore, it is important to emphasize that the sample was not exposed to a dynamic vacuum during the dehydrogenation kinetics measurements. Therefore, the slight decrease in the hydrogen absorption capacity could also be

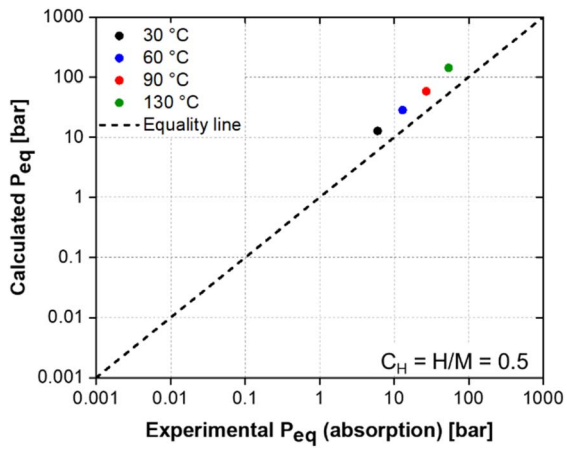

Fig. 7 Comparison between calculated and experimental (measured in absorption) equilibrium pressure for the $(Ti_{0.5}Zr_{0.5})_1(Fe_{0.33}Mn_{0.33}Cr_{0.33})_2$ alloy with c_H = H/M = 0.5 at 30 °C, 60 °C, 90 °C and 130 °C.

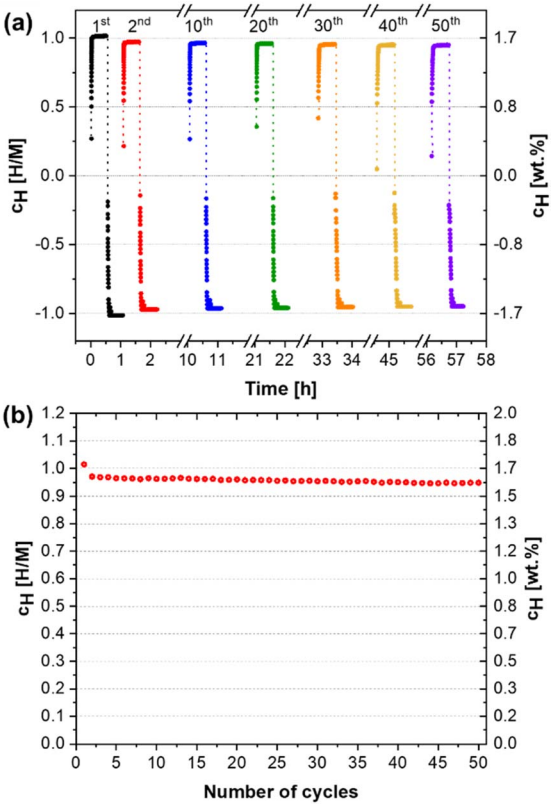

Fig. 8 Hydrogen absorption capacity in H/M and wt% of the $(Ti_{0.5}Zr_{0.5})_1(Fe_{0.33}Mn_{0.33}Cr_{0.33})_2$ alloy over the (a) 1st, 2nd, 10th, 20th, 30th, 40th, and 50th cycles of absorption and desorption, and (b) over all fifth cycles of absorption. During the absorption cycles, the initial hydrogen pressure was 52 bar, and the final pressure was 48 bar, approximately.

related to the remaining hydrogen in the crystal under cycling measurements.

The hydrogen absorption capacities of the alloy for the 50 cycles are presented in Fig. 8(b). After the second cycle, a slight decrease in hydrogen absorption from 1.62 wt% to 1.59 wt% (H/M = 0.94) was observed during the subsequent cycles, which indicates that the alloy can store at least 93% of its initial capacity after 50 cycles. Therefore, the alloy exhibits excellent reversible hydrogen storage properties. Furthermore, no kinetics damage was observed over the 50 hydrogen absorption/desorption cycles. The kinetics curves show that the material absorbs and desorbs hydrogen extremely fast and reaches its total hydrogen capacity in less than a minute for all the cycles. Fig. S4 in the ESI† shows the absorption and desorption curves in a different format evidencing the fast kinetics. The absorption kinetics acquisition provides essential information about the transformation of the material into a hydride, such as time, temperature, and pressure conditions. However, investigating these parameters for the reverse situation, *i.e.*, when the hydride returns to its metallic form, is equally relevant and rarely reported. Therefore, the desorption kinetics study in this work provided new insights into desorption behavior, which is a critical factor from the application point of view.

In terms of hydrogen absorption capacity, this alloy presents an excellent performance since the capacity is very similar to the calculated theoretical capacity for the AB_2H_3 hydride (1.67 wt%). This alloy performance can be considered comparable or superior to those reported for many C14 Laves phase alloys, which are often observed to be close to H/M = 1.[5–8,15,27–32] For example, Edalati *et al.*[5] reported that the equiatomic TiZrCrMnFeNi multicomponent alloy has a hydrogen absorption capacity of 1.70 wt% (H/M = 1) in the first cycle. Floriano *et al.*[6] showed that the $Ti_{20}Zr_{20}Nb_5Fe_{40}Ni_{15}$ alloy absorbs 1.38 wt% (H/M = 0.95) in the first cycle.

Furthermore, in terms of cyclability, the excellent performance of this alloy is also comparable to the few reported studies on the cycling of C14 Laves phase alloys. Li *et al.*[15] reported a maximum hydrogen absorption of 1.80 wt% for the $Ti_{0.8}Zr_{0.2}Mn_{0.9}Cr_{0.6}V_{0.3}Fe_{0.2}$ alloy with a slight decline in the first cycles, where a stabilization was reached with a capacity of 1.71 wt% over ten cycles. However, it is worth mentioning that in this case, the desorption was carried out by increasing the temperature to 400 °C under a dynamic vacuum for 30 min. Zhou *et al.*[27] showed that the absorption capacity of the $Ti_{0.8}Zr_{0.2}Cr_{0.75}Mn_{1.25}Ce_{0.02}$ alloy increased from 1.89 wt% to 1.98 wt% in the first cycles and then remained unchanged over 15 cycles. In this case, the desorption was carried out at 25 °C, but under a dynamic vacuum for 20 min. Chen *et al.*[33] observed in their study of the equiatomic TiZrFeMnCrV alloy a maximum hydrogen absorption capacity of 1.80 wt% for the first cycle that decreased to 1.76 wt% in the second cycle and remained practically constant over the subsequent 50 cycles. Again, the desorption was performed at high temperatures (350 °C) under a dynamic vacuum for 30 min. Thus, the room-temperature cycling stability of the $(Ti_{0.5}Zr_{0.5})_1(Fe_{0.33}Mn_{0.33}Cr_{0.33})_2$ is very impressive since practically the total hydrogen storage capacity of the alloy can be cycled without the need of increasing temperature or applying vacuum for hydrogen release.

In order to confirm that the alloy maintains its excellent hydrogen storage properties after cycling, the sample was subjected to an additional PCI test at 30 °C after the 50th cycle. The resulting PCI curve is shown in Fig. 9. Comparing the PCI curve of the cycled alloy with that before cycling, it is possible to confirm that no damage to the absorption/desorption capacity of the alloy was observed. After cycling, a slight increase in the total capacity, from 1.75 wt% (H/M = 1.04) to 1.81 (H/M = 1.08), was observed. Up to a pressure of approximately 60 bar, the PCI curve obtained after cycling showed a slightly lower absorption compared to the PCI of the uncycled sample. However, with the progressive increase in pressure up to 100 bar, the sample showed increased hydrogen absorption capacity.

Fig. 10 shows the microstructural characteristics of the $(Ti_{0.5}Zr_{0.5})_1(Fe_{0.33}Mn_{0.33}Cr_{0.33})_2$ alloy in three conditions. Fig. 10(a) and (d) show the as-cast sample after being crushed into powder (used to load into a Sieverts-type apparatus) in two different magnifications. The particle size of the alloy is in the range of about 200 μm. Fig. 10(b) and (e) show the sample after one hydrogen absorption and desorption cycle. As observed, the alloy particle size is obviously reduced, and cracks have appeared on the surface of the particles. Similar behavior was observed in previous studies and was related to the volume expansion of the C14 Laves phase after hydrogen absorption. This expansion generates a high internal stress concentration in the host metal. It leads to its embrittlement after absorption, resulting in a powder with a fine particle size of 10 to 100 μm.[15,34,35] An even greater particle size refinement and several cracks on the surface of the particles can be seen in Fig. 10(c) and (f), corresponding to the sample after 50 cycles of hydrogen absorption and desorption. As mentioned before, this reduction in at least one order of magnitude in the size of the alloy particles increases crystalline defects, such as dislocations and grain boundaries, contributing to the slight reduction of capacity during cycling.

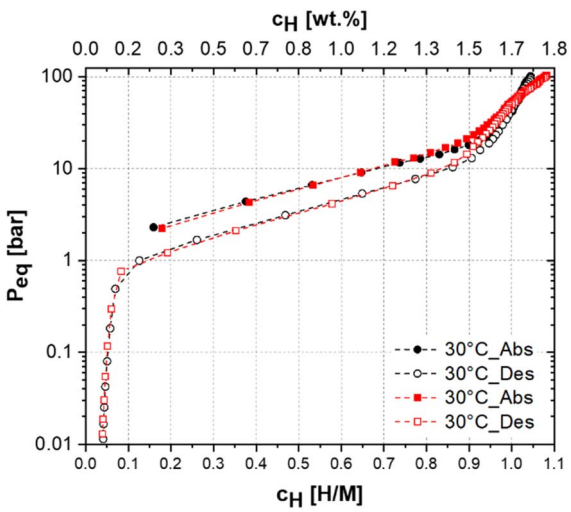

Fig. 9 PCI of $(Ti_{0.5}Zr_{0.5})_1(Fe_{0.33}\cdot Mn_{0.33}Cr_{0.33})_2$ alloy at 30 °C before (in black) and after (in red) 50 cycles of hydrogen absorption/desorption.

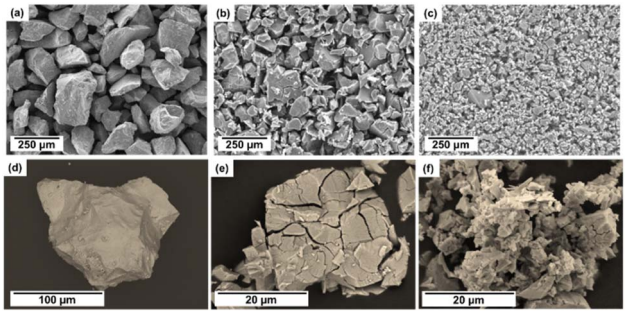

Fig. 10 SEM images of the $(Ti_{0.5}Zr_{0.5})_1(Fe_{0.33}Mn_{0.33}Cr_{0.33})_2$ alloy in as cast (a) and (d), after one hydrogenation/dehydrogenation cycle (b) and (e), and after 50th cycles of hydrogenation/dehydrogenation (c) and (f).

The microstructure of the as-cast $(Ti_{0.5}Zr_{0.5})_1(Fe_{0.33}Mn_{0.33}Cr_{0.33})_2$ alloy, and after the first and fiftieth cycles was further investigated by SEM equipped with EDX, and the results are shown in Fig. S5–S7 of the ESI.† No changes were observed in the chemical composition and distribution of the elements after the hydrogen absorption and desorption cycles to which the samples were subjected.

To better understand the hydrogen storage behavior of the $(Ti_{0.5}Zr_{0.5})_1(Fe_{0.33}Mn_{0.33}Cr_{0.33})_2$ alloy, the samples after the first and the 50th cycle of absorption and desorption were characterized by XRD. Fig. 11 shows the XRD patterns of these samples and the XRD pattern of the as-cast sample. The complete Rietveld refinements of these XRD patterns are presented in Fig. 3 for the as-cast samples and in Fig. S8 of the ESI† for the samples after the first and 50th cycles of absorption and desorption. The lattice parameters obtained by Rietveld refinement for the C14 Laves phase in these three samples are also shown in Fig. 11.

One can see that even after the hydrogenation cycles, no change was observed in the samples in terms of the constituent phase. After one and fifty hydrogenation cycles, the samples still presented a single C14 Laves phase, and no changes in lattice parameters were observed. These XRD results, PCI curves in Fig. 6, and the cycling test curves in Fig. 8 show that most of the hydrogen is easily desorbed from $(Ti_{0.5}Zr_{0.5})_1(Fe_{0.33}Mn_{0.33}Cr_{0.33})_2$ alloy when the hydrogen pressure is reduced to 1 bar. It is important to note that the alloy was almost entirely desorbed (H/M < 0.1) during the cycling test at room temperature and at an initial hydrogen pressure of 0.6 bar. The same procedure was applied during the PCT tests, *i.e.*, the practically full desorption (H/M < 0.05) was successfully carried out at the same temperature as the absorption (30 °C, 60 °C, 90 °C, and 130 °C) with the pressure-reducing steps down to 0.01 bar. In addition, the hydrogen remaining in the alloy structure was released during the evacuation of the sample prior to the further characterization of the alloy. Therefore, the characterization of the hydrogenated phase by XRD was not possible after the hydrogenation test.

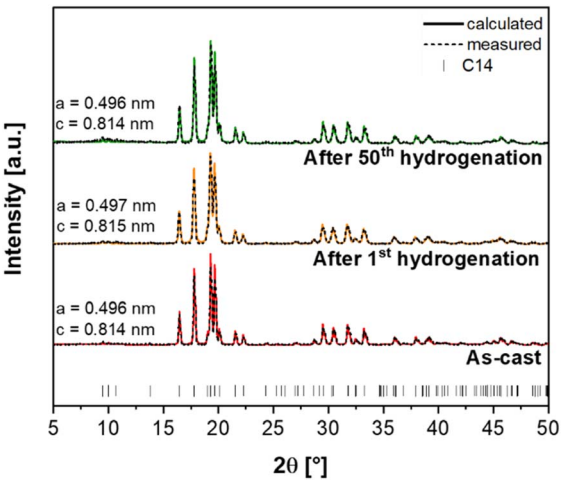

Fig. 11 XRD patterns of the $(Ti_{0.5}Zr_{0.5})_1(Fe_{0.33}Mn_{0.33}Cr_{0.33})_2$ alloy. (a) as cast, (b) after one absorption/desorption cycle, and (c) after fifty absorption/desorption cycles.

The transport sector is undoubtedly the field with the most significant potential to widen the use of systems based on hydrogen energy. The rising concerns about the dwindling resources of conventional energy and the environmental issues regarding fossil energy sources have promoted great efforts in developing systems to enable hydrogen-powered vehicles. In 2006, Toyota's group demonstrated the use of $Ti_{1.1}MnCr$ alloys in a high-pressure MH tank with a very high hydrogen absorption plateau pressure. The maximum storage capacity of 1.9 wt% has been reached only for a hydrogen pressure of around 350 bar at room temperature.[36] In 2015, Toyota's group launched the hydrogen fuel-cell-driven automobile adopting two 700 bar high-pressure hydrogen storage tanks, presenting a hydrogen density of 5.7 wt%.[37] However, the high operating pressure of the hydrogen storage tank raises safety and cost issues, and hydrogen storage technology remains a significant obstacle to implementing hydrogen-powered vehicles. On the other side, as reported in some studies, multicomponent alloys have presented other critical problems for various applications, such as poor reversibility, hysteresis, the need for activations procedure, and high temperature to complete absorption or desorption.[6,11] Recently, AB_2-type Ti–Zr–Cr-based alloy was optimized for a hybrid hydrogen storage tank of a fuel cell bicycle and showed a hydrogen storage capacity of 1.82 wt% under a hydrogen pressure of around 11 bar at room temperature.[28]

In this scenario, the development of hydrogen storage tanks operating at room temperature has considerable potential to enable the safe and cost-effective use of hydrogen-based energy systems in stationary and mobile applications. Following the set of properties that an alloy needs to have to be used in a solid-state hydrogen storage tank operating at room temperatures and mild pressure conditions, such as high hydrogen storage capacity, good absorption and desorption kinetics, cycling stability, reversibility, and equilibrium pressure just above atmospheric pressure, this comprehensive study evidenced that the $(Ti_{0.5}Zr_{0.5})_1(Fe_{0.33}Mn_{0.33}Cr_{0.33})_2$ alloy designed through computational thermodynamic tools is an excellent option for this application.

Conclusions

This study systematically investigated the $(Ti_{0.5}Zr_{0.5})_1(Fe_{0.33}Mn_{0.33}Cr_{0.33})_2$ alloy for hydrogen storage application. We have demonstrated that designing an alloy with specific hydrogen storage properties is possible using computational tools and the recently proposed thermodynamic model. A C14-type Laves phase alloy with promising room-temperature hydrogen storage properties was designed in this case.

In addition, the PCT-C14 model predicted a high tendency towards reversibility at room temperature due to the calculated hydrogen equilibrium pressure in the order of magnitude of 10^1 bar. Finally, the alloy was synthesized by arc-melting and experimentally evaluated in terms of its structure and hydrogen storage performance by structural and volumetric techniques.

The alloy presented a single C14 Laves phase, as the design strategy and CALPHAD calculation predicted. Under hydrogen pressure at room temperature, the alloy reached a total hydrogen storage capacity equal to 1.71 wt% (H/M = 1.02) in less than one minute, demonstrating fast absorption kinetics.

The PCT diagrams demonstrated that the alloy could reversibly absorb and desorb significant amounts of hydrogen under moderate temperatures and in the pressure range of 0 to 100 bar. Moreover, the PCT-C14 model reasonably predicted the order of magnitude of the experimental hydrogen equilibrium pressure for a given temperature.

The alloy showed excellent cycling stability with a hydrogen absorption of 1.59 wt% (H/M = 0.94) after 50 cycles, exhibiting superb reversible hydrogen storage properties. The structural characterization of the alloy after the hydrogenation/dehydrogenation cycles demonstrated that the single C14 Laves phase and its lattice parameters remain unaltered over cycling.

Author contributions

Jéssica Bruna Ponsoni: conceptualization, methodology, investigation, formal analysis, validation, data curation, writing – original Draft, writing – review & editing. Mateusz Balcerzak: methodology, investigation, validation, supervision, writing – review & editing. Walter José Botta: resources, acquisition, writing – review & editing. Michael Felderhoff: supervision, resources, writing – review & editing. Guilherme Zepon: conceptualization, methodology, validation, supervision, resources, funding acquisition, writing – original draft, writing – review & editing.

Conflicts of interest

There are no conflicts to declare.

Acknowledgements

This work was financed in part by the Serrapilheira Institute (grant number Serra-1709-17362) and in part by the Brazilian National Council for Scientific and Technological Development – CNPq (grant number: 309467/2021-7 and 407906/2022-3). This study was also financed in part by the Coordenação de Aperfeiçoamento de Pessoal de Nível Superior – Brasil (CAPES) – Finance Code 001, Federal University of Sao Carlos, Graduate Program in Materials Science and Engineering. The authors would like to acknowledge the help of the scientists from the Chemical Crystallography and Electron Microscopy Department and the financial support from the Max-Planck-Institute. Open Access funding provided by the Max Planck Society.

References

1 L. Schlapbach and A. Züttel, Hydrogen-storage materials for mobile applications, *Nature*, 2001, **414**, 353–358.
2 M. Hirscher, V. A. Yartys, M. Baricco, J. Bellosta von Colbe, D. Blanchard, R. C. Bowman, D. P. Broom, C. E. Buckley, F. Chang, P. Chen, Y. W. Cho, J. C. Crivello, F. Cuevas, W. I. F. David, P. E. de Jongh, R. V. Denys, M. Dornheim, M. Felderhoff, Y. Filinchuk, G. E. Froudakis, D. M. Grant, E. M. A. Gray, B. C. Hauback, T. He, T. D. Humphries, T. R. Jensen, S. Kim, Y. Kojima, M. Latroche, H. W. Li, M. V. Lototskyy, J. W. Makepeace, K. T. Møller, L. Naheed, P. Ngene, D. Noréus, M. M. Nygård, S. ichi Orimo, M. Paskevicius, L. Pasquini, D. B. Ravnsbæk, M. Veronica Sofianos, T. J. Udovic, T. Vegge, G. S. Walker, C. J. Webb, C. Weidenthaler and C. Zlotea, Materials for hydrogen-based energy storage – past, recent progress and future outlook, *J. Alloys Compd.*, 2020, **827**, 153548.
3 F. Marques, M. Balcerzak, F. Winkelmann, G. Zepon and M. Felderhoff, Review and outlook on high-entropy alloys for hydrogen storage, *Energy Environ. Sci.*, 2021, **14**, 5191–5227.
4 F. Stein and A. Leineweber, Laves phases: a review of their functional and structural applications and an improved fundamental understanding of stability and properties, *J. Mater. Sci.*, 2021, **56**, 5321–5427.
5 P. Edalati, R. Floriano, A. Mohammadi, Y. Li, G. Zepon, H. W. Li and K. Edalati, Reversible room temperature hydrogen storage in high-entropy alloy TiZrCrMnFeNi, *Scr. Mater.*, 2020, **178**, 387–390.
6 R. Floriano, G. Zepon, K. Edalati, G. L. B. G. Fontana, A. Mohammadi, Z. Ma, H. W. Li and R. J. Contieri, Hydrogen storage in TiZrNbFeNi high entropy alloys, designed by thermodynamic calculations, *Int. J. Hydrogen Energy*, 2020, **45**, 33759–33770.
7 V. Charbonnier, H. Enoki, K. Asano, H. Kim and K. Sakaki, Tuning the hydrogenation properties of $Ti^{1+}Cr_2$-Mn laves phase compounds for high pressure metal-hydride compressors, *Int. J. Hydrogen Energy*, 2021, **46**, 36369–36380.
8 S. K. Chen, P. H. Lee, H. Lee and H. T. Su, Hydrogen storage of C14-CruFevMnwTixVyZrz alloys, *Mater. Chem. Phys.*, 2018, **210**, 336–347.
9 V. A. Yartys and M. V. Lototskyy, Laves Type Intermetallic Compounds As Hydrogen Storage Materials: A Review, *J. Alloys Compd.*, 2022, 165219.
10 S. B. Gesari, M. E. Pronsato, A. Visintin and A. Juan, Hydrogen storage in AB_2 Laves phase (A = Zr, Ti; B = Ni,

Mn, Cr, V): binding energy and electronic structure, *J. Phys. Chem. C*, 2010, **114**, 16832–16836.

11 J.-G. Park, H.-Y. Jang, S.-C. Han, P. S. Lee and J.-Y. Lee, The thermodynamic properties of Ti–Zr–Cr–Mn Laves phase alloys, *J. Alloys Compd.*, 2001, **325**, 293–298.

12 P. Ma, W. Li and E. Wu, Hydrogen activation and storage properties of laves phase $Ti_{1-x}Sc_xMn_{1.6}V_{0.4}$ alloys, *Int. J. Hydrogen Energy*, 2021, **46**, 34389–34398.

13 X. Guo, S. Wang, X. Liu, Z. Li, F. Lü, J. Mi, L. Hao and L. Jiang, Laves phase hydrogen storage alloys for super-high-pressure metal hydride hydrogen compressors, *Rare Met.*, 2011, **30**, 227–231.

14 Z. Peng, Q. Li, J. Sun, K. Chen, W. Jiang, H. Wang, J. Liu, L. Ouyang and M. Zhu, Ti–Cr–Mn–Fe-based alloys optimized by orthogonal experiment for 85 MPa hydrogen compression materials, *J. Alloys Compd.*, 2022, **891**, 161791.

15 Z. Li, Y. Yan, H. Huang, B. Liu, Y. Lv, B. Zhang, W. Lv, J. Yuan and Y. Wu, Effects of the different element substitution on hydrogen storage properties of $Ti_{0.8}Zr_{0.2}Mn_{0.9}Cr_{0.6}V_{0.3}M_{0.2}$ (M = Fe, Ni, Co), *J. Alloys Compd.*, 2022, **908**, 164605.

16 M. Kandavel, V. V. Bhat, A. Rougier, L. Aymard, G. A. Nazri and J. M. Tarascon, Improvement of hydrogen storage properties of the AB_2 Laves phase alloys for automotive application, *Int. J. Hydrogen Energy*, 2008, **33**, 3754–3761.

17 J. B. Ponsoni, V. Aranda, T. da S. Nascimento, R. B. Strozi, W. J. Botta and G. Zepon, Design of multicomponent alloys with C14 laves phase structure for hydrogen storage assisted by computational thermodynamic, *Acta Mater.*, 2022, **240**, 118317.

18 J. H. Zhu, P. K. Liaw and C. T. Liu, Effect of electron concentration on the phase stability of $NbCr_2$-based Laves phase alloys, *Mater. Sci. Eng. A.*, 1997, **239–240**, 260–264.

19 V. F. Gorban', N. A. Krapivka and S. A. Firstov, High-entropy alloys: interrelations between electron concentration, phase composition, lattice parameter, and properties, *Phys. Met. Metallogr.*, 2017, **118**, 970–981.

20 S. S. Mishra, T. P. Yadav, O. N. Srivastava, N. K. Mukhopadhyay and K. Biswas, Formation and stability of C14 type Laves phase in multi component high-entropy alloys, *J. Alloys Compd.*, 2020, **832**, 153764.

21 F. Stein, M. Palm and G. Sauthoff, Structure and stability of Laves phases. Part I. Critical assessment of factors controlling Laves phase stability, *Intermetallics*, 2004, **12**, 713–720.

22 N. Yurchenko, N. Stepanov and G. Salishchev, Laves-phase formation criterion for high-entropy alloys, *Mater. Sci. Technol.*, 2017, **33**, 17–22.

23 G. Zepon, B. H. Silva, C. Zlotea, W. J. Botta and Y. Champion, Thermodynamic modelling of hydrogen-multicomponent alloy systems: calculating pressure-composition-temperature diagrams, *Acta Mater.*, 2021, **215**, 117070.

24 V. Zadorozhnyy, B. Sarac, E. Berdonosova, T. Karazehir, A. Lassnig, C. Gammer, M. Zadorozhnyy, S. Ketov, S. Klyamkin and J. Eckert, Evaluation of hydrogen storage performance of ZrTiVNiCrFe in electrochemical and gas-solid reactions, *Int. J. Hydrogen Energy*, 2020, **45**, 5347–5355.

25 R. Griessen and T. Riesterer, *Heat of Formation Models*, 1988, pp. 219–284.

26 B. H. Toby and R. B. Von Dreele, GSAS-II: the genesis of a modern open-source all purpose crystallography software package, *J. Appl. Crystallogr.*, 2013, **46**, 544–549.

27 L. Zhou, W. Li, H. Hu, H. Zeng and Q. Chen, Ce-Doped TiZrCrMn Alloys for Enhanced Hydrogen Storage, *Energy Fuels*, 2022, **36**, 3997–4005.

28 B. Tu, H. Wang, Y. Wang, R. Li, L. Ouyang and R. Tang, Optimizing Ti–Zr–Cr–Mn–Ni–V alloys for hybrid hydrogen storage tank of fuel cell bicycle, *Int. J. Hydrogen Energy*, 2022, **47**, 14952–14960.

29 E. Akiba and H. Iba, Hydrogen absorption by Laves phase related BCC solid solution, *Intermetallics*, 1998, **6**, 461–470.

30 I. Kunce, M. Polanski and J. Bystrzycki, Structure and hydrogen storage properties of a high entropy ZrTiVCrFeNi alloy synthesized using Laser Engineered Net Shaping (LENS), *Int. J. Hydrogen Energy*, 2013, **38**, 12180–12189.

31 K. H. Young, J. Nei, C. Wan, R. V. Denys and V. A. Yartys, Comparison of C14-and C15-predominated AB 2 metal hydride alloys for electrochemical applications, *Batteries*, 2017, **3**, 22.

32 B. Sarac, V. Zadorozhnyy, E. Berdonosova, Y. P. Ivanov, S. Klyamkin, S. Gumrukcu, A. S. Sarac, A. Korol, D. Semenov, M. Zadorozhnyy, A. Sharma, A. L. Greer and J. Eckert, Hydrogen storage performance of the multi-principal-component CoFeMnTiVZr alloy in electrochemical and gas–solid reactions, *RSC Adv.*, 2020, **10**, 24613–24623.

33 J. Chen, Z. Li, H. Huang, Y. Lv, B. Liu, Y. Li, Y. Wu, J. Yuan and Y. Wang, Superior cycle life of TiZrFeMnCrV high entropy alloy for hydrogen storage, *Scr. Mater.*, 2022, **212**, 114548.

34 A. Züttel, Materials for hydrogen storage, *Mater. Today*, 2003, **6**, 24–33.

35 M. Dornheim, Thermodynamics of metal hydrides: tailoring reaction enthalpies of hydrogen storage materials, *Thermodynamics – Interaction Studies – Solids, Liquid and Gases*, 2011, 33, pp. 891–918.

36 Y. Kojima, Y. Kawai, S. ichi Towata, T. Matsunaga, T. Shinozawa and M. Kimbara, Development of metal hydride with high dissociation pressure, *J. Alloys Compd.*, 2006, **419**, 256–261.

37 A. Yamashita, M. Kondo, S. Goto and N. Ogami, *Development of High-Pressure Hydrogen Storage System for the Toyota "Mirai"*, SAE Tech. Pap. 2015-01-1169, 2015.

